



1 On the relationship between the mesospheric sodium layer and the meteoric input function

2 **Yanlin Li<sup>1</sup>, Tai-Yin Huang<sup>2</sup>, Julio Urbina<sup>1</sup>, Fabio Vargas<sup>3</sup>, Wuhu Feng<sup>4</sup>**

3 1. Department of Electrical Engineering, Pennsylvania State University, University Park, PA, USA

4 2. Department of Physics, Penn State Lehigh Valley, Center Valley, PA, USA

5 3. Department of Electrical Engineering, University of Illinois Urbana-Champaign, Champaign, IL, USA

6 4. National Centre for Atmospheric Science, University of Leeds, Leeds, UK

7 *Correspondence to:* Tai-Yin Huang (tuh4@psu.edu)

8

9

## 10 **Abstract**

11

12 This study examines the relationship between the concentration of atmospheric sodium and its  
13 Meteoric Input Function (MIF). We use the measurements from the Colorado State University (CSU)  
14 Lidar and the Andes Lidar Observatory (ALO) with a new numerical model that includes sodium  
15 chemistry in the mesosphere and lower thermosphere (MLT) region. The model is based on the  
16 continuity equation to treat all sodium-bearing species and runs at a high temporal resolution. The  
17 model simulation employs data assimilation to compare the MIF inferred from the meteor radiant and  
18 the MIF derived from the new sodium chemistry model. The simulation captures the seasonal variability  
19 of sodium number density compared with lidar observations over the CSU site. However, there were  
20 discrepancies for the ALO site, which is close to the South Atlantic Anomaly (SAA) region, indicating it is  
21 challenging for the model to capture the observed sodium over ALO. The CSU site had significantly more  
22 lidar observations (27,930 hours) than the ALO sites (1872 hours). The simulation revealed that the  
23 uptake of the sodium species on meteoric smoke particles was a critical factor in determining the  
24 sodium concentration in MLT, with the sodium removal rate by uptake found to be approximately three  
25 times that of the NaHCO<sub>3</sub> dimerization. Overall, the study's findings provide valuable information on the  
26 correlation between MIF and sodium concentration in the MLT region, contributing to a better  
27 understanding of the complex dynamics in this region. This knowledge can inform future research and  
28 guide the development of more accurate models to enhance our comprehension of the MLT region's  
29 behavior.

30

31 **Keywords:** Sodium layer, sodium chemistry, Meteor radiant distribution, Meteoroid input function

32

### 33 **Key points:**

34

35

36

37

38

39

40

- A high-time resolution, time-dependent Na chemistry model is developed.
- Ablated global meteoroid material inputs inferred from ALO and CSU observations are 116.85 t d<sup>-1</sup> and 61.4 t d<sup>-1</sup>, respectively.
- Meteoroid material input by mass and by occurrence may differ.



## 41 1. Introduction

42 Micro-meteoroids enter the Earth's atmosphere day and night, depositing their constituents into the  
43 atmosphere via ablation, creating a region that hosts various metal species, for example, Fe, K, Si, Mg,  
44 Ca, and Na, in both neutral and ion form (Plane et al., 2015; Plane et al., 2021; and references therein).  
45 The region is commonly referred to as the mesosphere and lower thermosphere (MLT), located between  
46 75 and 110 km altitude. The metal layers in the MLT often serve as the tracers that facilitate the  
47 investigation of the dynamical and chemical processes within the region (Takahashi et al., 2014; Qiu et  
48 al., 2021). Quantitative measurements of metal atoms have been made since the 1950s (Hunten, 1967)  
49 through a variety of ground or space-borne technologies (Julia et al., 2022). The large resonant  
50 scattering cross-section (Bowman et al., 1969) and the substantial presence of the sodium atom in the  
51 MLT make it one of the most researched metal layers in the atmosphere (Yu et al., 2022).

52 The sodium layer is usually studied via observations carried out by resonance lidars, satellites, and  
53 through Na D-line emission at 589.0nm and 589.6nm (Plane, 2010; Plane et al., 2012; Hedin and  
54 Gumbel, 2011; Langowski et al., 2017; Andrioli et al., 2019; Li et al., 2020a). The sodium vertical profiles  
55 retrieved by lidars have been commonly used as a tracer to study atmospheric dynamics, e.g., gravity  
56 waves, wind shear, etc. The long-term seasonal and short-term diurnal variability of metallic species  
57 have been investigated by several studies (Feng et al., 2013; Marsh et al., 2013; Cai et al., 2019a, b; Yu et  
58 al., 2022). A typical sodium chemistry scheme consists of neutral chemistry, ion chemistry, and  
59 photolysis. The sodium chemistry research in recent years has primarily been based on the sodium  
60 chemistry model by Plane (2004), which has been cited in various subsequent works, including Bag et al.  
61 (2015) and references therein.

62 As meteoroids are the primary source of metal layers in the atmosphere, including the sodium layer,  
63 the Meteoroid Input Function (MIF) plays a crucial role in the modeling of metallic layers in the  
64 atmosphere. Sporadic meteors are estimated to make up more than 95% of the total meteoroid  
65 population by comparing the number of meteors originating in sporadic sources to those originating in  
66 known shower meteor sources (Chau and Galindo, 2008). This highlights the importance of  
67 incorporating sporadic meteor data in the MIF to accurately understand sodium concentration in the  
68 mesosphere and lower thermosphere (MLT) region and its correlation with meteoroid material input.  
69 It's well established that there are six apparent sources of sporadic meteors, namely North and South  
70 Apex (NA and SA); North and South Toroidal (NT and ST); and Helion and Anti-Helion sources (H and AH)  
71 (Campbell-Brown, 2008; Kero et al., 2012; Li et al., 2022). However, the relative strength of these  
72 meteor radiant sources varies among the studies. For example, the NA and SA sources are found to be  
73 much stronger than other sources in results obtained with High Power Large Aperture (HPLA) radars  
74 (Chau et al., 2007; Kero et al., 2012; Li and Zhou, 2019), while specular meteor radars found the  
75 difference to be much smaller (Campbell-Brown and Jones, 2005; Campbell-Brown, 2008). The detection  
76 sensitivity varies among different facilities by several orders of magnitude, as evidenced by Arecibo  
77 Observatory (AO, 18° N. 66° W) detecting about 20 times more meteors per unit area per unit time than  
78 the Jicamarca Radio Observatory (JRO, 12°S 77°W) despite both being HPLA facilities with similar radar  
79 pulse schemes (Li et al., 2020).

80 Consequently, the radiant mass distribution of the meteors that enter the Earth's atmosphere is subject  
81 to significant uncertainties. In the existing WACCM-Na global sodium model (Dunker et al., 2015), the  
82 meteor input function was modeled by placing a flux curve on each radiant meteor source with a



83 definite ratio (more details can be found in Marsh et al., 2013). The flux curve model is based on  
84 observations carried out exclusively by the Arecibo Observatory. Although the model can reproduce  
85 some of the flux characteristics of the meteors observed at Arecibo, it is a relatively simple model and  
86 therefore has several limitations (Li et al., 2022). One of the limitations is that the model cannot  
87 reproduce the velocity distribution of the meteors in observations.

88 This study introduces a new numerical model for sodium chemistry that utilizes the continuity equations  
89 for all Na-related reactions without steady-state approximations. The main objective is to investigate the  
90 relationship between the apparent sodium concentration and the Meteoroid Input Function (MIF) in the  
91 MLT region. We then compare the results of the new model with measurements from two lidar  
92 instruments, namely the Colorado State University (CSU) and the Andes Lidar Observatory (ALO).  
93 Additionally, we compare the MIF obtained from the new sodium chemistry model with the results of  
94 the high-resolution meteor radiant distribution recently inferred from observations made with the  
95 Arecibo Observatory. Finally, we discuss the implications of these comparisons and suggest possible  
96 explanations for the observed discrepancy between the MIF derived from radar and those obtained  
97 from lidar observations.

98

## 99 **2. The sodium chemistry model (NaChem)**

### 100 **2.1 Sodium chemistry**

101 Numerical airglow models have been extensively used to investigate atmospheric airglow chemistry and  
102 gravity waves (Huang and Hickey, 2008; Huang and Richard, 2014; Huang, 2015). A new numerical  
103 sodium chemistry model, hereafter referred to as NaChem, was developed for this study. Table 1 lists  
104 the complete reactions and their corresponding rate coefficients used in NaChem, which includes  
105 neutral chemistry, ion chemistry, and photochemistry. The dimerization reaction of  $\text{NaHCO}_3$  (reaction 25  
106 in Table 1) is the outlet that removes Na atoms in the chemistry scheme. The Na atoms can also be  
107 removed by the uptake of sodium species onto meteoric smoke particles (Hunten et al., 1980;  
108 Kalashnikova et al., 2000; Plane, 2004), a process that can be turned on or off in the model. This study  
109 estimates the MIF in the numerical model by matching the dimerization reaction to maintain the  
110 observed sodium present in the MLT. Throughout the rest of the paper, the MIF estimated from the  
111 sodium chemistry numerical model will be referred to as MIF(s). On the other hand, the MIF derived  
112 from meteor radiant distribution will be referred to as MIF(m). The MIF(m) is determined through a 3-D  
113 meteoroid orbital simulation based on the meteor radiant distribution.

114 The numerical model utilizes the continuity equation to track the time evolution of all 14 Na-related  
115 species. Table 2 presents a comprehensive list of these species, along with their corresponding  
116 production and loss rates. The background major gas species, including  $\text{O}_3$ ,  $\text{O}_2$ , O, H,  $\text{H}_2$ ,  $\text{H}_2\text{O}$ , etc., and  
117 the temperature are provided by the Whole Atmosphere Community Climate Model (WACCM). Here we  
118 use the dynamic version of WACCM nudged with NASA's Modern Era Retrospective Analysis for  
119 Research and Application MERRA2 reanalysis data set (Hunziker & Wendt, 1974; Molod et al., 2015;  
120 Gettelman et al., 2019). The WACCM reference profiles are linearly interpolated to a resolution of one  
121 minute and updated every minute during the simulation. It is worth noting that the Na-related  
122 reactions, which are illustrated in Table 2, do not significantly impact the background gas species, as the



123 effect is orders of magnitude smaller than the variation of the major gas species themselves. Therefore,  
124 the major gas species are simulated independently of Na-related reactions.

## 125 **2.2 Numerical scheme**

126 As discussed earlier, it is worth noting that the reactions of sodium chemistry in NaChem share  
127 similarities with those in previous models (e.g., Plane et al., 2015 and references therein); however, the  
128 implementation of the numerical chemistry scheme differs. NaChem uses continuity equations to treat  
129 all chemicals involved, including short-lived intermediate species. Treating all species with the continuity  
130 equation is a more straightforward yet accurate approach than using steady-state approximations.  
131 Moreover, by treating all species in a uniform procedure, the numerical model is more compact and  
132 easier to interpret. The computational capability of a personal computer nowadays has advanced  
133 enough to process an ultra-fine time step (microseconds) that is necessary for numerical simulations of  
134 short-lived species in a reasonable duration. Still, the differential equations for production and loss of  
135 short-lived species can be numerically unstable unless microsecond or even sub-microsecond time step  
136 is used (Higham, 2002). The concern of the differential equation instability can be largely mitigated by a  
137 first-order exponential integrator (Hochbruck and Ostermann, 2010), i.e.,

138

$$c = x_0 - \frac{a_0}{b_0} \tag{1}$$
$$x_1 = \frac{a_0}{b_0} + ce^{-b_0\Delta t}$$

139

140 Where  $x_0$  is the value of the current step,  $a_0$  is the production of the species,  $b_0$  is the loss of the  
141 species,  $\Delta t$  is the step size in time, and  $x_1$  is the value of the next step.

142 The exponential integrator, expressed in Equation 1, provides the solution to the continuity equation,  
143 with the exception of reaction 25 listed in Table 1. It is worth noting that reaction 25 is the sole  
144 mechanism for removing Na from the chemistry simulation, apart from the uptake of sodium species.  
145 Nevertheless, our testing suggests that either the exponential integrator or explicit Euler integrator  
146 produces nearly identical results, however the explicit Euler integrator was running in four orders of  
147 magnitude smaller step size (1 $\mu$ s). The default time step of NaChem is 0.1 seconds with the exponential  
148 integrator.

149

150

151

152

153

154



155 Table 1. Reactions in NaChem.  $f_a$  and  $f_x$  are branching ratios.

	Reaction	Rate Coefficient	reference
<b>neutral chemistry</b>			
1	$\text{Na} + \text{O}_3 \rightarrow \text{NaO(A)} + \text{O}_2$	$K_1 = 1.1 \times 10^{-9} \exp(-116/T)$	1
2	$\text{NaO(A)} + \text{O} \rightarrow \text{Na}^{(2)\text{P}} + \text{O}_2$	$K_2 = 2.2 \times 10^{-10} (T/200)^{0.5}$ , $f_a = 0.14 \pm 0.4$	1,3
3	$\text{NaO(A)} + \text{O} \rightarrow \text{Na}^{(2)\text{S}} + \text{O}_2$	$K_3 = 2.2 \times 10^{-10} (T/200)^{0.5}$ , $(1-f_a)$	1,3
4	$\text{NaO(A)} + \text{O}_2 \rightarrow \text{NaO(X)} + \text{O}_2$	$K_4 = 1 \times 10^{-11}$	1
5	$\text{Na} + \text{O}_2 + \text{M} \rightarrow \text{NaO}_2 + \text{M}$	$K_5 = 5.0 \times 10^{-30} (200/T)^{1.22}$	1
6	$\text{NaO}_2 + \text{O} \rightarrow \text{NaO(X)} + \text{O}_2$	$K_6 = 5 \times 10^{-10} \exp(-940/T)$	1
7	$\text{NaO(X)} + \text{O} \rightarrow \text{Na}^{(2)\text{P}} + \text{O}_2$	$K_7 = 2.2 \times 10^{-10} (T/200)^{0.5}$ , $f_x = 0.167$	1,2
8	$\text{NaO(X)} + \text{O} \rightarrow \text{Na}^{(2)\text{S}} + \text{O}_2$	$k_8 = 2.2 \times 10^{-10} (T/200)^{0.5}$ , $(1-f_x)$	1,2
9	$\text{NaO(X)} + \text{O}_3 \rightarrow \text{NaO}_2 + \text{O}_2$	$k_9 = 1.1 \times 10^{-9} \exp(-568/T)$	1
10	$\text{NaO(X)} + \text{O}_3 \rightarrow \text{Na} + 2\text{O}_2$	$k_{10} = 3.2 \times 10^{-10} \exp(-550/T)$	1
11	$\text{NaO(X)} + \text{O}_2 + \text{M} \rightarrow \text{NaO}_3 + \text{M}$	$k_{11} = 5.3 \times 10^{-30} (200/T)$	1
12	$\text{NaO(X)} + \text{H} \rightarrow \text{Na} + \text{OH}$	$k_{12} = 4.4 \times 10^{-10} \exp(-668/T)$	1
13	$\text{NaO(X)} + \text{H}_2 \rightarrow \text{NaOH} + \text{H}$	$k_{13} = 1.1 \times 10^{-9} \exp(-1100/T)$	1
14	$\text{NaO(X)} + \text{H}_2 \rightarrow \text{Na} + \text{H}_2\text{O}$	$k_{14} = 1.1 \times 10^{-9} \exp(-1400/T)$	1
15	$\text{NaO(X)} + \text{H}_2\text{O} \rightarrow \text{NaOH} + \text{OH}$	$k_{15} = 4.4 \times 10^{-10} \exp(-507/T)$	1
16	$\text{NaO(X)} + \text{CO}_2 + \text{M} \rightarrow \text{NaCO}_3 + \text{M}$	$K_{16} = 1.3 \times 10^{-27} (200/T)$	1
17	$\text{NaO}_2 + \text{H} \rightarrow \text{Na} + \text{HO}_2$	$K_{17} = 1.0 \times 10^{-9} \exp(-1000/T)$	1
18	$\text{NaO}_3 + \text{O} \rightarrow \text{Na} + 2\text{O}_2$	$K_{18} = 2.5 \times 10^{-10} (T/200)^{0.5}$	1
19	$\text{NaCO}_3 + \text{O} \rightarrow \text{NaO}_2 + \text{CO}_2$	$K_{19} = 5.0 \times 10^{-10} \exp(-1200/T)$	1
20	$\text{NaCO}_3 + \text{H} \rightarrow \text{NaOH} + \text{CO}_2$	$k_{20} = 1.0 \times 10^{-9} \exp(-1400/T)$	1
21	$\text{NaOH} + \text{H} \rightarrow \text{Na} + \text{H}_2\text{O}$	$k_{21} = 4.0 \times 10^{-11} \exp(-550/T)$	1
22	$\text{NaOH} + \text{CO}_2 + \text{M} \rightarrow \text{NaHCO}_3 + \text{M}$	$k_{22} = 1.9 \times 10^{-28} (200/T)^{\dagger}$	1
23	$\text{NaHCO}_3 + \text{H} \rightarrow \text{Na} + \text{H}_2\text{O} + \text{CO}_2$	$k_{23} = 1.1 \times 10^{-11} \exp(-910/T)$	1
24	$\text{NaHCO}_3 + \text{H} \rightarrow \text{Na} + \text{H}_2\text{CO}_3$	$K_{24} = 1.84 \times 10^{-13} T^{0.777} \exp(-1014/T)$	1
25	$2\text{NaHCO}_3 + \text{M} \rightarrow (\text{NaHCO}_3)_2 + \text{M}$	$K_{25} = 8.8 \times 10^{-10} \exp(T/200)^{-0.23}$	1
26	$\text{Na}^{(2)\text{P}} \rightarrow \text{Na}^{(2)\text{S}} + h\nu(589.0-589.6 \text{ nm})$	$K_{26} = 6.26 \times 10^7$	1
<b>ion-molecule chemistry</b>			
27	$\text{Na} + \text{O}_2^+ \rightarrow \text{Na}^+ + \text{O}_2$	$K_{27} = 2.7 \times 10^{-9}$	1
28	$\text{Na} + \text{NO}^+ \rightarrow \text{Na}^+ + \text{NO}$	$K_{28} = 8.0 \times 10^{-10}$	1
29	$\text{Na}^+ + \text{N}_2 + \text{M} \rightarrow \text{NaN}_2^+ + \text{M}$	$k_{29} = 4.8 \times 10^{-30} (T/200)^{-2.2}$	1
30	$\text{Na}^+ + \text{CO}_2 + \text{M} \rightarrow \text{NaCO}_2^+ + \text{M}$	$k_{30} = 3.7 \times 10^{-29} (T/200)^{-2.9}$	1
31	$\text{NaN}_2^+ + \text{O} \rightarrow \text{NaO}^+ + \text{N}_2$	$k_{31} = 4.0 \times 10^{-10}$	1
32	$\text{NaO}^+ + \text{N}_2 \rightarrow \text{NaN}_2^+ + \text{O}$	$k_{32} = 1.0 \times 10^{-12}$	1
33	$\text{NaO}^+ + \text{O} \rightarrow \text{Na}^+ + \text{O}_2$	$K_{33} = 1.0 \times 10^{-11}$	1
34	$\text{NaO}^+ + \text{O}_2 \rightarrow \text{Na}^+ + \text{O}_3$	$K_{34} = 5.0 \times 10^{-12}$	1
35	$\text{NaN}_2^+ + \text{X} \rightarrow \text{NaX}^+ + \text{N}_2$ (X=CO <sub>2</sub> , H <sub>2</sub> O)	$K_{35} = 6.0 \times 10^{-10}$	1
36	$\text{NaY}^+ + \text{e} \rightarrow \text{Na} + \text{Y}$ (Y=N <sub>2</sub> , CO <sub>2</sub> , H <sub>2</sub> O, O)	$k_{36} = 1.0 \times 10^{-6} (T/200)^{-0.5}$	1
<b>photochemical reactions</b>			
37	$\text{NaO(A)}/\text{NaO(X)} + h\nu \rightarrow \text{Na} + \text{O}$	$K_{37} = 5.5 \times 10^{-2}$	1
38	$\text{NaO}_2 + h\nu \rightarrow \text{Na} + \text{O}_2$	$K_{38} = 1.9 \times 10^{-2}$	1
39	$\text{NaOH} + h\nu \rightarrow \text{Na} + \text{OH}$	$K_{39} = 1.8 \times 10^{-2}$	1
40	$\text{NaHCO}_3 + h\nu \rightarrow \text{Na} + \text{HCO}_3$	$K_{40} = 1.3 \times 10^{-4}$	1
41	$\text{Na} + h\nu \rightarrow \text{Na}^+ + \text{e}^-$	$K_{41} = 2 \times 10^{-5}$	1

156 \*1:Plane (2004), 2: Plane (2012), 3: Griffin et al. (2001).

157



158 Table 2. The production and loss terms of the sodium-related species.

	Species	Prod	Loss
a1	Na(2P)	$k_2[a_3][O] + k_7[a_5][O];$	1*
a2	Na	$k_3[a_3][O] + k_8[a_5][O] + k_{10}[a_5][O_3] + k_{12}[a_5][H] + k_{14}[a_5][H_2] + k_{17}[a_4][H] + k_{18}[a_6][O] + k_{21}[a_7][H] + k_{23}[a_9][H] + k_{24}[a_9][H] + k_{36}[a_{11}][e] + k_{36}[a_{13}][e] + k_{36}[a_{12}][e] + k_{36}[a_{14}][e] + [a_1] + k_{37}[a_3][hv] + k_{37}[a_5][hv] + k_{38}[hv][a_4] + k_{39}[hv][a_7] + k_{40}[hv][a_9];$	$k_1[O_3] + k_5[O_3] + k_5[O_2][M] + k_{27}[O_2^*] + k_{28}[NO^*] + k_{41}[hv];$
a3	NaO(A)	$k_1[a_2][O_3]$	$k_2[O] + k_3[O] + k_4[O_2] + k_{37}[hv]$
a4	NaO <sub>2</sub>	$k_5[a_2][O_2][M] + k_9[a_5][O_3] + k_{19}[a_8][O]$	$k_6[O] + k_{17}[H] + k_{38}[hv]$
a5	NaO(X)	$k_5[a_2][O_2] + k_4[a_3][O_2] + k_6[a_4][O]$	$k_7[O] + k_8[O] + k_9[O_3] + k_{10}[O_3] + k_{11}[O_2][M] + k_{12}[H] + k_{13}[H_2] + k_{14}[H_2] + k_{15}[H_2O] + k_{16}[CO_2][M] + k_{37}[hv]$
a6	NaO <sub>3</sub>	$k_{11}[a_5][O_2][M]$	$k_{18}[O]$
a7	NaOH	$k_{13}[a_5][H_2] + k_{15}[a_5][H_2O] + k_{20}[a_8][H]$	$k_{21}[H] + k_{22}[CO_2][M] + k_{39}[hv]$
a8	NaCO <sub>3</sub>	$k_{16}[a_5][CO][M]$	$k_{19}[O] + k_{20}[H]$
a9	NaHCO <sub>3</sub>	$k_{22}[a_7][CO_2][M]$	$k_{23}[H] + k_{24}[H] + 2k_{25}[a_9][M] + k_{40}[hv]$
a10	Na <sup>+</sup>	$k_{27}[a_2][O_2^*] + k_{28}[a_2][NO^*] + k_{33}[a_{13}][O] + k_{34}[a_{13}][O_2] + k_{41}[hv][a_2]$	$k_{29}[N_2][M] + k_{30}[CO_2][M]$
a11	NaN <sub>2</sub> <sup>+</sup>	$k_{29}[a_{10}][N_2][M] + k_{32}[a_{13}][N_2]$	$k_{31}[O] + k_{35}[CO_2] + k_{35}[H_2O] + k_{36}[e]$
a12	NaCO <sub>2</sub> <sup>+</sup>	$k_{30}[a_{10}][CO_2][M] + k_{35}[a_{11}][CO_2]$	$k_{36}[e]$
a13	NaO <sup>+</sup>	$k_{31}[a_{11}][O]$	$k_{32}[N_2] + k_{33}[O] + k_{34}[O_2] + k_{36}[e]$
a14	NaH <sub>2</sub> O <sup>+</sup>	$k_{35}[a_{11}][H_2O]$	$k_{36}[e]$

159

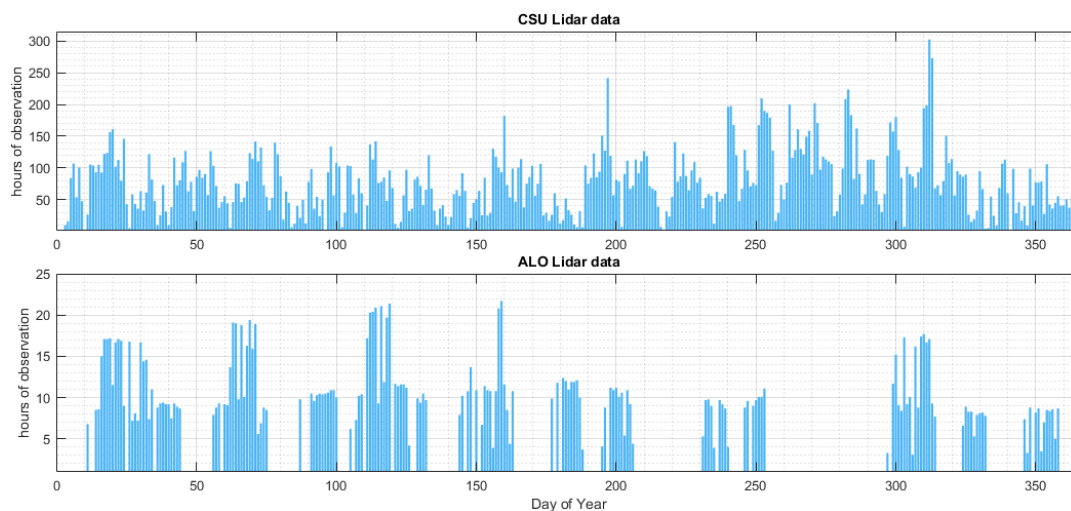
160 \*In Species 1, as of the current state of the model, all Na(2p) atoms return to their ground state  
 161 immediately, so the loss term is set to 1. The [hv] is the term that represents loss via photon emission,  
 162 which follows a sinusoidal function based on the zenith angle of the respective local time.

163

### 164 3. CSU and ALO Sodium Lidar Observations and data processing

#### 165 3.1 Observations

166 Several aspects of the current research, i.e., the presence of sodium in the MLT, require cross-validation  
 167 with the measurements. One primary objective of the present model is to match the observed seasonal  
 168 variation of the sodium layer. Measurements by the Colorado State University (CSU, 41.4°N, 111.5°W)  
 169 Lidar, formerly known as Utah State University (USU) Lidar, and the lidar data acquired by the Andes  
 170 Lidar Observatory (ALO, 30.3°S, 70.7°W), are used to facilitate the research in the current study. We are  
 171 unable to acquire more ALO data after 2019 as the COVID situation disrupted the site operation.. It  
 172 contains a total of 27,930 hours of lidar observations carried out between 1990 and 2020, whereas the  
 173 ALO data consists of 1872 hours between 2014 and 2019.



174

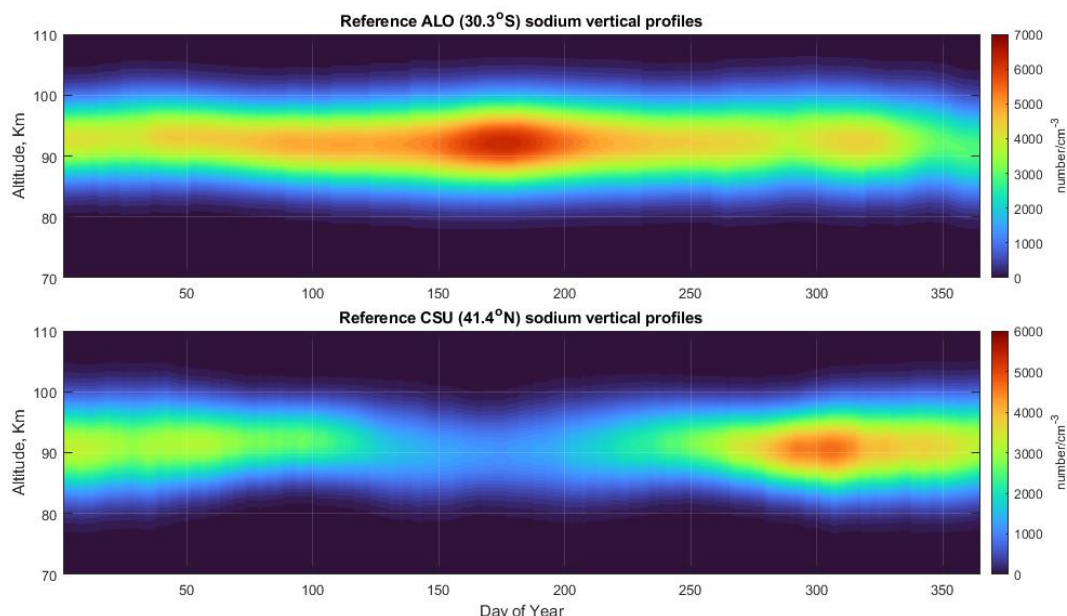
175 **Figure 1.** CSU lidar data from 1990 to 2020 (top plot) and ALO lidar data from 2014 to 2019 (bottom  
176 plot).

177 The statistics of CSU and ALO available data are presented in Figure 1. The Lidar observations of both  
178 sites consist of nocturnal observations only, and a typical nocturnal observation lasts between 8 and 11  
179 hours. Note that in Figure 1, there could be as many as 300 hours of sodium observations on a single day  
180 of year, which means the data of the date comprise observations of many years on that day in different  
181 years. The CSU data almost covered every day of the year with only a few exceptions, whereas the ALO  
182 data was much more sparse. As a result, due to the significantly larger number of CSU observations, the  
183 statistical reliability of the seasonal variation in the sodium layer derived from ALO observations may not  
184 be as strong as that of the CSU data. The general seasonal trend of the sodium vertical profile retrieved  
185 from the CSU lidar observations is similar to the estimation by simulation made by Marsh et al. (2013),  
186 whereas the results of ALO lidar observations differ from the Marsh et al. results.

187

### 188 **3.2 Data processing**

189 The sodium layer in atmospheric observations is often affected by perturbations of atmospheric  
190 dynamics, which is why sodium is commonly used as a tracer in the study of the MLT dynamics (Plane et  
191 al., 2015). However, studying the sodium layer itself can be complicated due to the underlying chemical  
192 processes coupled with the dynamics. In order to mitigate the effects of atmospheric dynamics, we  
193 process the sodium vertical profiles from observations in three steps. First, we average the profiles by  
194 day of the year, meaning we take the average of the data from the same day of the year from different  
195 years. Missing data are treated using linear interpolation. Next, we smooth the averaged profiles using a  
196 15-day running average. Finally, we further smooth the profiles by fitting them with a skew-normal  
197 distribution using the least squares error method.



198

199 **Figure 2.** *The reference annual sodium vertical profiles at ALO (top plot) and at CSU (bottom plot). The*  
200 *reference profiles are the averages throughout all the available data on the same days at the respective*  
201 *site, then fitted by a normal distribution that mitigates atmospheric dynamics. In essence, the reference*  
202 *profiles are measurements with small-scale dynamics removed via steps discussed in section 3.2.*

203

204 Figure 2 displays the processed annual sodium vertical profiles. These vertical profiles are used as the  
205 reference for the model to fit with and provide the background conditions for deriving the required  
206 meteor input function. The reference profiles used in the NaChem sodium chemistry numerical model  
207 inherently account for the effects of diffusion of sodium species as these observational data are the  
208 snapshots of sodium in diffusion at any given time. By constantly matching the observed Na profile to  
209 the simulated Na profile, the diffusion is included implicitly in the model. The seasonal column densities  
210 of both ALO and CSU profiles are similar to a sinusoidal function, with ALO data peaking near June and  
211 CSU data peaking in November. The centroid height of the sodium layer is higher in the ALO data than in  
212 the CSU data.

213

## 214 **4. Results**

### 215 **4.1 Sensitivity test**

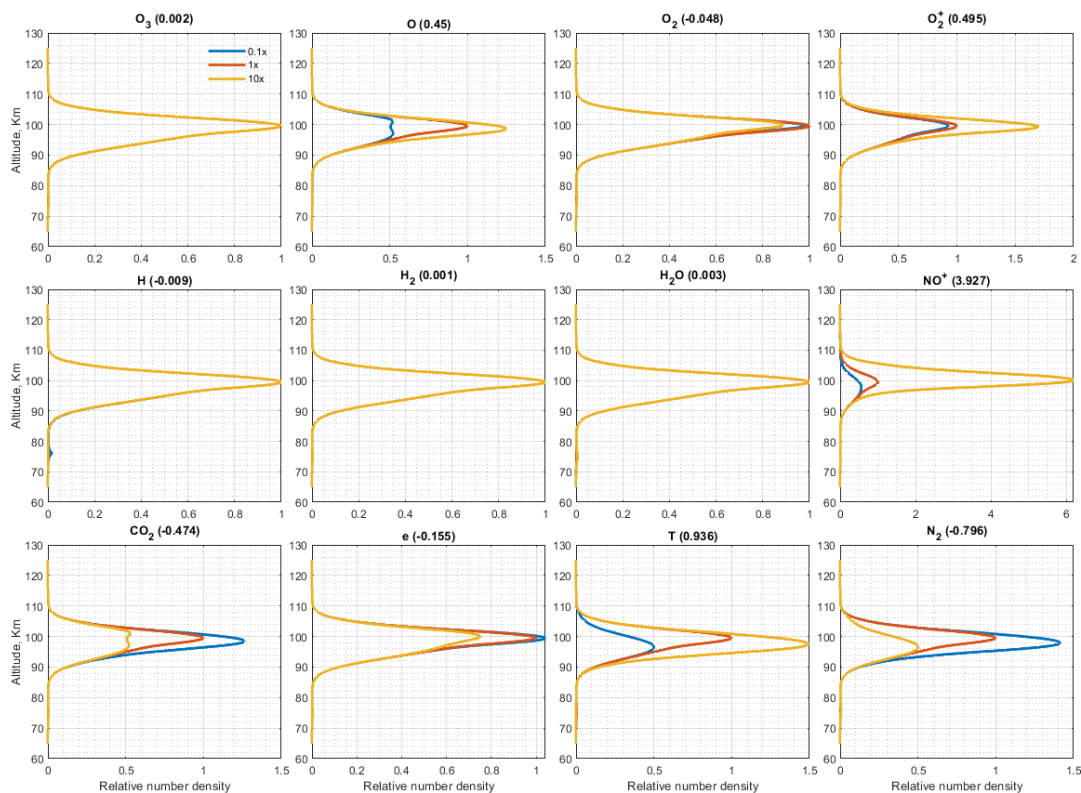
216 Sodium in the atmosphere could manifest in many forms, i.e., in sodium-bearing neutral chemicals and  
217 ionic chemicals. The sodium number densities are typically obtained via lidar measurements. Given the  
218 complexity of the sodium chemistry, the observed sodium is merely a subset, possibly not even a major  
219 constituent, of the total number of all the sodium-bearing species in the atmosphere. The total sodium  
220 content is defined as the total number of sodium atoms in all 14 sodium-bearing species, as listed in





221 Table 2. It is important to note that the observable sodium does not necessarily well represent the total  
 222 sodium content or the total number of sodium-bearing species, as non-observable species like  $\text{Na}^+$  and  
 223  $\text{NaHCO}_3$  may constitute a substantial portion of the total sodium content.

224 Understanding the impact of each background species, i.e., species listed in Figure 3., to the share of Na  
 225 atom to the total sodium content is essential to study the underlying mechanism of the chemical  
 226 reactions. Therefore, we present a sensitivity test by isolating variables. The sensitivity test is done by  
 227 altering the number density of background species in question by two orders of magnitude, i.e., with a  
 228 factor of 0.1 and 10, while keeping the number densities of other background species and sodium fixed.  
 229 The simulation is kept running until all the numbers are stable. The results of the sensitivity test of the  
 230 11 background species and temperatures involved in the numerical simulation are shown in Figure 3.  
 231 Each panel contains three lines, where the red curve shows the unaltered vertical profile of the total  
 232 sodium content. The results of the species altered by the factor of 0.1 and 10 are shown in light blue and  
 233 yellow, respectively.



234

235 **Figure 3.** Sensitivity test of 11 background species and temperature on Na chemistry. The total sodium  
 236 content vertical profile for the respective background species altered by 10x and 0.1x are shown in  
 237 yellow and light blue. The reference sodium content vertical profiles are shown in red. The numbers in  
 238 the parentheses are the sensitivity factor. More about the sensitivity factor can be found in equation (2)  
 239 and the corresponding discussion.



240

241 In Figure 3, only the yellow curve is visible in some of the panels because the three curves are drawn on  
242 top of each other, indicating that the change of the respective background species bears little to no  
243 effect on the sodium chemistry. A sensitivity factor is defined to better quantify the weight of each  
244 background species in sodium chemistry. The factor is measured by the following equation:

$$245 \quad \text{Sensitivity Factor} = \frac{NaT_c^{10} - NaT_c^{0.1}}{NaT_c} \quad (2)$$

246 Where  $NaT_c^{10}$  is the column density of the total sodium content with the respective specie altered by a  
247 factor of 10, and  $NaT_c^{0.1}$  is the same operation as the previous one but altered by a factor of 0.1. The  
248 denominator,  $NaT_c$ , is the column density of the reference profile. For example, a Sensitivity Factor (SF)  
249 of 5 indicates that the total sodium content increases by five times when the respective background  
250 species increases 100 times. A positive sensitivity factor indicates the total sodium content is positively  
251 correlated to the respective species and vice versa. The reference profile is the total sodium content in  
252 steady-state in the background condition of the midnight new year of 2002, giving a typical sodium  
253 vertical profile similar to the one shown in Figure 5 of Plane (2004). In the simulation, a greater total  
254 sodium content implies that a smaller percentage of the sodium chemicals are present as sodium atoms  
255 as the altitude profile of the sodium atoms is fixed. In reality, instead of the sodium atoms, the total  
256 sodium content should be more or less conserved. Hence a higher total sodium content in our  
257 simulation suggests less sodium can be detected by the lidar.

258 Although the sensitivity factor could be different upon the change of the reference profile, it still gives  
259 an insight into the significance of each background species to the sodium chemistry. Apparently, the  
260 weight of some background species, namely O<sub>3</sub>, H, H<sub>2</sub>, and H<sub>2</sub>O, is negligible in sodium chemistry,  
261 meaning that removing these species and their associated reactions has no effect on the overall sodium  
262 chemistry. Nevertheless, these species are still kept in our numerical model for completeness. The  
263 impact of species that converts Na atom to Na<sup>+</sup>, as listed in reactions 27 and 28 of Table 1, is generally  
264 strong. The effect of NO<sup>+</sup>, in particular, is the most significant according to the sensitivity factor, greater  
265 than the combined effect of all the other species. Consequently, the number density of the sodium atom  
266 by lidar observation is strongly correlated with the fluctuations of the NO<sup>+</sup>. In a nutshell, more NO<sup>+</sup> will  
267 directly lead to fewer observable Na atoms. That being said, the works of the background species are in  
268 a rather complex pattern. The scope of the sensitivity test in the present paper was limited to column  
269 density. As a result of such, variations and behaviors of the sodium chemicals by altitude are overlooked.  
270 The actual impact of the background species may differ at different altitudes.

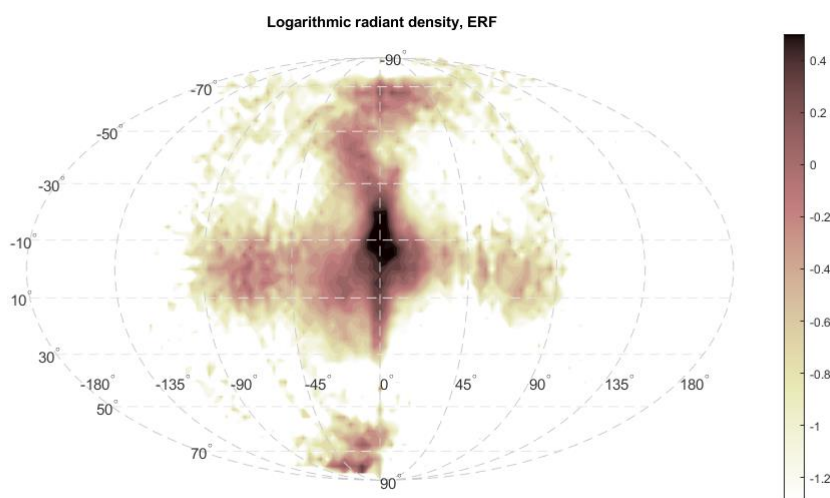
#### 271 **4.2 Meteor input function**

272 The estimation of meteoric influx is subject to many uncertainties among different techniques (Li et al.,  
273 2022). Moreover, the meteor flux estimated by the sodium chemistry model also varies (Marsh et al.,  
274 2014; Plane et al., 2015). The previous model of Plane (2004) and the following similar models indicate  
275 that the rate of dimerization, or the speed of removing sodium from the system, is heavily correlated to  
276 the vertical transport in the MLT. The NaChem model does not explicitly incorporate vertical transport,  
277 but the vertical transport by diffusion is inherently embedded within the input of the observed sodium  
278 vertical profile.



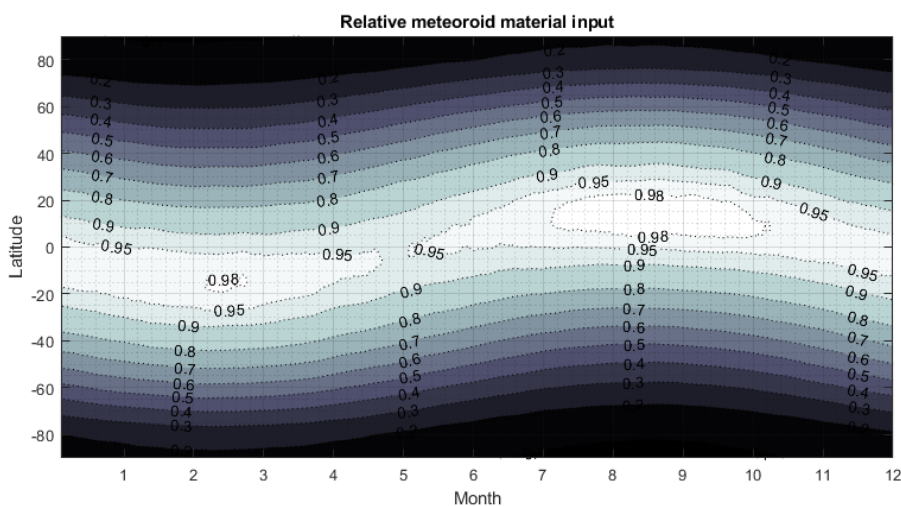
279 Unlike the previous models (Plane 2004; March et al. 2014; and references therein), the present  
280 NaChem model took an indirect route to estimate the meteor mass input. During the simulation, the  
281  $\text{NaHCO}_3$  dimerization and the uptake of the sodium species, which can be turned on or off, create a  
282 deficit of sodium atoms. Meanwhile, a meteor input function injects an appropriate amount of sodium  
283 atoms so that the present sodium vertical profile always matches the reference profiles. This is carried  
284 out by finding the difference between the current sodium profile (with the deficit) and the  
285 corresponding reference profile in every iteration and then replacing the former with the latter. The  
286 diffusion coefficient is found to be highly correlated with the sink rate of the dimerization reaction with  
287 large uncertainties (Plane, 2004). The simulation bypasses such uncertainty by directly using the  
288 observational sodium vertical profile, as the diffusion should already be infused within.

289



290

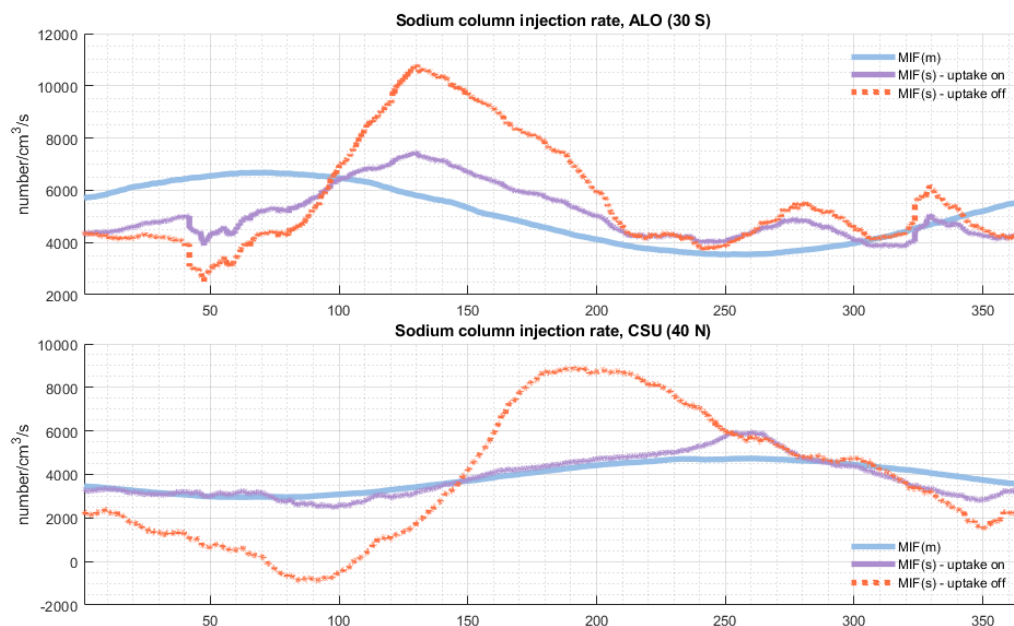
291 **Figure 4.** Meteor radiant source derived from the AO observations. The result is in the Earth Reference  
292 Frame (ERF), equivalent to ground-based observations. The radiant distribution is derived from the  
293 number of meteor events. Figure reproduced from Li et al. (2022).



294

295 **Figure 5.** Relative seasonal and latitudinal meteoroid input, inferred from the radiant source distribution  
296 shown in Figure 4.

297



298

299 **Figure 6.** A comparison between two meteor input functions: MIF(m), which is inferred from micro-  
300 meteor radiant distribution, and MIF(s), which is derived using a Na chemistry model. The purple line  
301 represents MIF(s) with uptake on, while the orange dotted line represents MIF(s) with uptake off.

302



303 Figure 4 shows the high-resolution meteor radiant source distribution recently inferred from the AO  
304 observations (Li et al., 2022). The typical mass of the Arecibo meteors is estimated to be around  $10^{-13}$  Kg  
305 based on flux rate (Li and Zhou, 2019). Mathews et al. (2001) estimated the limiting meteor mass of  $10^{-14}$   
306 Kg based on the meteor ballistic parameter. Despite these estimations being based on various simplified  
307 assumptions that may lead to inaccurate results, the estimated mass is still at least two orders of  
308 magnitude smaller than the estimations of other facilities by similar means. More than 95% of the  
309 meteoroid population in the Earth's atmosphere is found to be sporadic meteors by HPLA radar  
310 observation (Chau and Galindo, 2007), which typically are low-mass meteors evolved from the outer  
311 Solar system due to the Poynting-Robertson drag (Nesvorn'y et al., 2011; Koschny et al., 2019). That  
312 being said, the percentage of sporadic meteors, as well as the radiant source distribution, are both  
313 estimated based on the occurrence. However, the occurrence of sporadic meteors may not be able to  
314 represent their mass distribution. The relative seasonal and latitudinal meteoroid input by the number  
315 of events inferred from the new radiant distribution is depicted in Figure 5. The meteoroid input  
316 generally follows a sinusoidal pattern and differs from the one used in the previous work, as shown in  
317 Figure 1 of Marsh et al. (2013). Although the interplanetary dust (meteor) background on the Earth's  
318 orbit could vary in different locations due to a variety of reasons, e.g., Jupiter resonance, it is still safe to  
319 assume no change in the interplanetary dust background for our purpose. Taking a stable interplanetary  
320 dust background, the MIF(m) 's seasonal sinusoidal pattern should follow the Earth's axis rotation.

321 Figure 6 shows a comparison between two types of meteor input function: MIF(m), which is inferred  
322 from the micro-meteor radiant distribution, and MIF(s), which is derived using the Na chemistry model  
323 with sodium input from the lidar observations. For the MIF(s) model simulations, we did two scenarios,  
324 one with and one without uptakes by smoke particles, for the ALO and CSU data. The MIF(s) with uptake  
325 by smoke particles exhibit a good match with the MIF(m) on the CSU dataset, while it does not show as  
326 good of a match on the ALO dataset. The MIF(s) with smoke uptake on is represented by a purple line,  
327 while the MIF(s) with smoke uptake turned off is depicted by an orange dotted line. The MIF(s) could go  
328 negative when the reference sodium vertical profile decreases faster than the removal rate by the  
329 dimerization, as shown in the orange dotted line in Figure 6, indicating that the dimerization process  
330 alone is not sufficient enough to account for all the sodium atom depletion in the MLT region. MIF(m) is  
331 derived from a global micro-meteor radiant distribution model, as depicted in Figure 4 and Figure 5. The  
332 smoke uptake of sodium species in this study is implemented using a methodology similar to Plane  
333 (2004), but instead of applying smoke uptake solely to the three major sodium species, namely Na,  
334 NaHCO<sub>3</sub>, and Na<sup>+</sup>, it is applied to all 14 sodium-bearing species. The optimal uptake factor to obtain the  
335 best results was found to be  $2 \times 10^{-2}$ /km/s. The smoke uptake and NaHCO<sub>3</sub> dimerization account for  
336 approximately 75% and 25% of the Na sink, respectively.

337 According to the global meteoroid orbital model outlined in (Li et al., 2022), the latitudes spanning 29.5°  
338 S to 30.5° S (ALO) account for 0.52% of the total meteor input, while those between 39.5° N and 40.5° N  
339 (CSU) represent 0.67%. The CSU site shares more meteor input due to its closer proximity to one of the  
340 Apex meteor radiant sources. The global total sodium injection rate inferred from the ALO data-based  
341 simulation is  $2.83 \times 10^{23}$  atoms per second, and the CSU-data-based simulation suggests a global sodium  
342 injection rate of  $1.49 \times 10^{23}$  atoms per second. Assuming the relative sodium elemental abundance in  
343 meteoroid material is 0.8% (Vondrak et al., 2008), the deduced total meteoroid material input of ALO-  
344 based simulation was  $116.85 \text{ t d}^{-1}$ . From CSU-based simulation, the rate is  $61.47 \text{ t d}^{-1}$ . Both estimations  
345 are close to 80-130  $\text{t d}^{-1}$ , the value reported by the Long Duration Exposure Facility (Love and Brownlee,



346 1993; McBride et al., 1999). It's worth noting that the estimated total daily input of meteoroid materials  
347 varies among previous studies, ranging from  $4.6 \text{ t d}^{-1}$  (Marsh et al., 2013) to  $300 \text{ t d}^{-1}$  (Nesvorný et al.,  
348 2009), with an intermediate value of  $20 \text{ t d}^{-1}$  reported by Carrillo-Sánchez et al. (2020). While these  
349 estimates seem quite disparate, the variance is relatively small given that the daily input rate is derived  
350 from combinations of chemicals that can fluctuate by several orders of magnitude.

351

## 352 5. Discussion

353 The sodium concentration in the sodium layer in the MLT region is governed by several factors, including  
354 chemistry, dynamics, and the MIF. It's difficult to discern which of these three components is more  
355 important than the others. In this section, we discuss various factors that may contribute to modeling  
356 the sodium concentration in the MLT.

357 The mass of the meteoroids, which constitute the metal layers in the MLT, has been estimated and  
358 measured by various means, e.g., ballistic parameter (Mathews et al. 2001); plasma by meteor ablation  
359 model, radar cross-section (Close et al., 2005; Sugar et al., 2021), flux rate (Zhou and Kelley, 1997), and  
360 spacecraft observations (Leinert and Grun, 1990), to name a few. The mass estimated by the meteor  
361 ballistic parameter is commonly referred to as momentum or dynamical mass. The mass estimated by  
362 the meteor ablation model is usually called the scattering mass. The meteor momentum mass from  
363 Arecibo Ultra-High-Frequency (UHF) radar observation is estimated to be  $10^{-14} - 10^{-7} \text{ kg}$ , with the typical  
364 mass being  $10^{-13} \text{ kg}$ . On the other hand, the meteor scattering mass is estimated to be  $10^{-9} - 10^{-5.5} \text{ kg}$  by  
365 data from EISCAT UHF radar (Kero et al., 2008) and  $10^{-7} - 10^{-4.5} \text{ kg}$  by data from ALTAIR UHF radar (Close  
366 et al., 2005). While the detection sensitivity among different facilities differs, these estimations are still  
367 off by many orders of magnitude. The assessments of either momentum mass or scattering mass are  
368 based on a variety of simplified assumptions. They are subject to errors due to the complexity of radar  
369 beam patterns, background atmosphere conditions, aspect sensitivity, meteor radiant sources, and  
370 many other possible factors. For example, radar meteor observation is subject to bias against low-mass,  
371 low-velocity meteors (Close et al., 2007; Janches et al., 2015).

372 Another aspect that may contribute to the MIF(m)'s uncertainty is the meteor radiant distribution. The  
373 meteor radiant distributions shown in Figure 4 and many others (Chau et al., 2004; Campbell-Brown and  
374 Jones, 2006; Kero et al., 2012) are inferred or measured by meteor occurrence instead of mass input.  
375 Currently, retrieving a more accurate estimation of the meteor mass input is still a topic under active  
376 research, and there is no quantitative study on the disparities between meteor occurrence and meteor  
377 mass input. The radiant sources of the meteors are expected to differ by mass as their orbital evolution  
378 is highly correlated to their mass. The interplanetary dust interacts with the solar wind while in the Solar  
379 System, losing its momentum in the process and evolving into orbits with a smaller semi-major axis and  
380 lower eccentricity. The effect is called the Poynting-Robertson effect (Robertson and Russell, 1937),  
381 which behaves like a drag force and defines the evolution of interplanetary dust, and it could be the  
382 major reason for the existence of sporadic meteors (Li and Zhou, 2019; Koschny et al., 2019). The  
383 importance of the Poynting-Robertson effect is highly dependent on the density and mass of the object.  
384 By and large, the orbits of the smaller particles evolve exponentially faster. The orbital dynamics of  
385 interplanetary particles have been very well summarized in section 2.2 of (Koschny et al., 2019). For the  
386 reasons above, the meteor radiant distribution of mass could deviate from the radiant distribution of  
387 occurrence. Therefore, the meteor input rates as shown in the blue curves of Figure 6 could be different



388 from those derived from the meteor radiant distribution of mass since they were derived from the  
389 meteor radiant distribution by occurrence.

390 In the sodium chemistry model presented in this work, the MIF is the sole source of sodium, while the  
391 sodium sink comprises  $\text{NaHCO}_3$  dimerization and smoke uptake. The MIF(s) is determined by matching  
392 the sink rate of the sodium atoms with the rate of sodium injection. In other words, MIF(s) represents  
393 the amount of sodium injection needed to keep the sodium concentration equal to the reference  
394 sodium profiles. If the chemical lifetime of sodium in the MLT is short, then the seasonal variation of  
395 both the MIF and sodium concentration in the MLT should be similar. After examining Figures 3, 5, and  
396 6, it can be observed that the averaged seasonal variation of sodium over the years at both sites (ALO  
397 and CSU) does not correspond to the trend of the MIF(m) at their respective latitudes. This may indicate  
398 that the chemical lifetime of sodium in the MLT should be relatively long, as there is no immediate effect  
399 of MIF(m) on the sodium concentration. The MIF displays a sinusoidal pattern which peaks in March at  
400 the ALO's latitude and in August at the CSU's latitude, whereas the sodium layer shows dual peaks in the  
401 CSU's lidar observations and one peak in June in the ALO's lidar observations.

402 In our simulation, the MIF(s) inferred by NaChem was consistent with the MIF(m) derived from the  
403 meteor radiant distribution. Although the model does not directly incorporate any dynamical processes,  
404 the vertical transport by diffusion would have been implicitly included. The model forces the sodium  
405 layer to be the same as the data, which are averaged by the observations of many years, in which the  
406 diffusions are inherently embedded. The combination of observational data with the numerical  
407 chemistry model in this paper is a relatively straightforward application of data assimilation (Bouttier &  
408 Courtier 2002). The lidar data of both sites (CSU and ALO) indicate that the sodium column density  
409 consistently increases by about 20% from 22:00 to 4:00 LT the next day. This can be attributed to the  
410 fact that, during nighttime, the large deposits of  $\text{Na}^+$  formed by daytime reactions slowly neutralized to  
411 Na. As a result, the sodium column density consistently increases throughout the night. The same effect  
412 can be reproduced in the NaChem simulation, albeit with a smaller amplitude. The simulation shows the  
413 increase to be about 8%. This number is obtained by turning the sodium sink off and keeping the total  
414 number of sodium in the system conserved.

415 While meridional transport or atmospheric dynamics both contribute to the seasonal variation of the  
416 sodium layer in the MLT, the diurnal sodium profile is the mean of observations of thousands of days, of  
417 which the variation by atmospheric dynamics should be much less prominent. The lack of explicit  
418 dynamics in the model may be one of the sources of inconsistency when compared to the observations.  
419 Further, the WACCM, which supplied the background species to the NaChem, is an older version that  
420 does not fully incorporate the dynamics of each ion species. Despite our results showing good  
421 agreement between the MIF(s) and the MIF(m), there might be several plausible factors that could lead  
422 to potential errors. For example, the Na sink by  $\text{NaHCO}_3$  dimerization varies by the diffusion rate or the  
423 vertical transport of sodium atoms in the chemistry model (Plane, 2004). Likewise, the MIF(m) may also  
424 differ if the meteoroid mass input differs from the radiant source distribution by the occurrence of  
425 meteors, as discussed in the aforementioned paragraph.

## 426 5. Conclusion

427 This work introduced a new sodium chemistry model that simulates the time evolution of all sodium-  
428 bearing species using the continuity equation without making any steady-state assumption. The model  
429 employs an exponential integrator and runs in high-time resolution to maintain numerical stability. The



430 model is simple to maintain in such a configuration and can be scaled up to include additional  
431 capabilities more easily. The model is highly optimized for processing efficiency and benefits from the  
432 use of an exponential integrator. Therefore, within an acceptable total CPU time, the NaChem can afford  
433 a time resolution of up to milliseconds, several orders of magnitude smaller than those used in other Na  
434 models. During our testing, the CPU time to simulated real-time ratio is about 1 to 100 using a 10-  
435 millisecond time step.

436 The model simulation was able to reproduce the seasonal variation of the sodium layer in the MLT by  
437 simulations of chemical reactions. The simulation results at the CSU's latitude capture the general trend  
438 of the seasonal variation at the location. The MIF(s) based on the ALO data exhibited less conformity  
439 with the corresponding MIF(m), which could be attributed to inadequate statistics of the observational  
440 data. Comparably, the CSU dataset is more reliable as the insufficient lidar hours in the ALO dataset may  
441 lead to inaccurate statistics. In the simulation, when forcing the sodium layer to be the observation-  
442 based reference profile, the inferred MIF is  $116.85 \text{ t d}^{-1}$  at ALO and  $61.47 \text{ t d}^{-1}$  at CSU. The numerical  
443 simulation by NaChem could reproduce the general trend of diurnal and seasonal variation of the  
444 sodium layer compared to the observations by the CSU Lidar. There are some inconsistencies in MIF(m)  
445 and MIF(s) based on data obtained from ALO Lidar. These inconsistencies may have originated from  
446 poor statistics resulting from insufficient observation hours.

447 In summary, a new sodium chemistry model has been developed in this work to investigate the  
448 relationship between MIF and the sodium layer. We also compared the MIF(m) derived from radar  
449 meteor observation to the MIF(s) derived from the chemistry model and lidar observations. Our results  
450 indicate that the uptake of sodium species onto meteoric smoke particles removes approximately three  
451 times more sodium than the dimerization of  $\text{NaHCO}_3$ . Our future work will focus on incorporating the  
452 plausible factors that may lead to potential errors discussed above into the chemistry model.

453

454

#### 455 Acknowledgment

456 The study is supported by NSF Grant AGS-1903346. T.-Y. Huang acknowledges that her work is supported  
457 by (while serving at) the National Science Foundation. WF was supported by the UK Natural Environment  
458 Research Council (grant no. NE/P001815/1). Any opinions, findings, and conclusions or recommendations  
459 expressed in this material are those of the authors and do not necessarily reflect the views of the National  
460 Science Foundation. The lidar data used in this paper are obtained from The Utah State University (USU)  
461 Sodium LIDAR facility and the Andes Lidar Observatory.

462

#### 463 Code/Data availability

464 The code and data used in this work are available upon request to Yanlin Li, [yxl875@psu.edu](mailto:yxl875@psu.edu).

465

#### 466 Author contribution

467 All authors have equal contributions to the work.





468 Competing interests

469 The authors declare no competing interests.

470

471 **Reference**

472 Andrioli, V., Xu, J., Batista, P., Pimenta, A., Resende, L., Savio, S., . . . others (2020). Nocturnal and  
473 seasonal variation of na and k layers simultaneously observed in the mlt region at 23 s. *Journal of*  
474 *Geophysical Research: Space Physics*, 125 (3), e2019JA027164.

475 Bag, T., Sunil Krishna, M., & Singh, V. (2015). Modeling of na airglow emission and first results on the  
476 nocturnal variation at midlatitude. *Journal of Geophysical Research: Space Physics*, 120 (12), 10–945.

477 Bowman, M., Gibson, A., & Sandford, M. (1969). Atmospheric sodium measured by a tuned laser radar.  
478 *Nature*, 221 (5179), 456–457.

479 Bouttier, F., & Courtier, P. (2002). Data assimilation concepts and methods March 1999. Meteorological  
480 training course lecture series. ECMWF, 718, 59.

481 Cai, X., Yuan, T., Eccles, J. V., Pedatella, N., Xi, X., Ban, C., & Liu, A. Z. (2019). A numerical investigation on  
482 the variation of sodium ion and observed thermospheric sodium layer at cerro pachon, chile during  
483 equinox. *Journal of Geophysical Research: Space Physics*, 124 (12), 10395–10414.

484 Cai, X., Yuan, T., Eccles, J. V., & Raizada, S. (2019). Investigation on the distinct nocturnal secondary  
485 sodium layer behavior above 95 km in winter and summer over logan, ut (41.7 n, 112 w) and arecibo  
486 observatory, pr (18.3 n, 67 w). *Journal of Geophysical Research: Space Physics*, 124 (11), 9610–9625.

487 Campbell-Brown, M. (2008). High resolution radiant distribution and orbits of sporadic radar  
488 meteoroids. *Icarus*, 196 (1), 144–163.

489 Campbell-Brown, M., & Jones, J. (2006). Annual variation of sporadic radar meteor rates. *Monthly*  
490 *Notices of the Royal Astronomical Society*, 367 (2), 709–716.

491 Carrillo-Sánchez, J. D., Bones, D. L., Douglas, K. M., Flynn, G. J., Wirick, S., Fegley Jr, B., ... & Plane, J.  
492 M. (2020). Injection of meteoric phosphorus into planetary atmospheres. *Planetary and Space*  
493 *Science*, 187, 104926.

494 Chau, J. L., & Galindo, F. (2008). First definitive observations of meteor shower particles using a high-  
495 power large-aperture radar. *Icarus*, 194 (1), 23–29.

496 Chau, J. L., Woodman, R. F., & Galindo, F. (2007). Sporadic meteor sources as observed by the jicamarca  
497 high-power large-aperture vhf radar. *Icarus*, 188 (1), 162–174.

498 Close, S., Brown, P., Campbell-Brown, M., Oppenheim, M., & Colestock, P. (2007). Meteor head echo  
499 radar data: Mass–velocity selection effects. *Icarus*, 186 (2), 547–556.

500 Close, S., Oppenheim, M., Durand, D., & Dyruud, L. (2005). A new method for determining meteoroid  
501 mass from head echo data. *Journal of Geophysical Research: Space Physics*, 110 (A9).



- 502 Dunker, T., Hoppe, U.-P., Feng, W., Plane, J. M., & Marsh, D. R. (2015). Mesospheric temperatures and  
503 sodium properties measured with the alomar na lidar compared with waccm. *Journal of Atmospheric*  
504 *and Solar-Terrestrial Physics*, 127 , 111–119.
- 505 Feng, W., Marsh, D. R., Chipperfield, M. P., Janches, D., Hoffner, J., Yi, F., & Plane, J. M. (2013). A global  
506 atmospheric model of meteoric iron. *Journal of Geophysical Research: Atmospheres*, 118 (16), 9456–  
507 9474.
- 508 Griffin, J., Worsnop, D., Brown, R., Kolb, C., & Herschbach, D. (2001). Chemical kinetics of the  $\text{NaO}^+$  ( $2\sigma^+$ ) +  $\text{O}^+$  ( $3p$ ) reaction (Vol. 105) (No. 9). ACS Publications.
- 510 Gettelman, A., Mills, M. J., Kinnison, D. E., Garcia, R. R., Smith, A. K., Marsh, D. R., ... & Randel, W. J.  
511 (2019). The whole atmosphere community climate model version 6 (WACCM6). *Journal of Geophysical*  
512 *Research: Atmospheres*, 124(23), 12380-12403.
- 513 Hedin, J., & Gumbel, J. (2011). The global mesospheric sodium layer observed by odin/osiris in 2004–  
514 2009. *Journal of atmospheric and solar-terrestrial physics*, 73 (14-15), 2221–2227.
- 515 Higham, N. J. (2002). Accuracy and stability of numerical algorithms. SIAM.
- 516 Hochbruck, M., & Ostermann, A. (2010). Exponential integrators. *Acta Numerica*, 19 , 209–286.
- 517 Huang, T.-Y., & Hickey, M. P. (2008). Secular variations of OH nightglow emission and of the OH  
518 intensity-weighted temperature induced by gravity-wave forcing in the MLT region. *Advances in Space*  
519 *Research*, doi:10.1016/j.asr.2007.10.020.
- 520 Huang, T.-Y. & George, R. (2014). Simulations of Gravity Wave-induced Variations of the OH(8,3),  
521 O<sub>2</sub>(0,1), and O(<sup>1</sup>S) Airglow Emissions in the MLT Region, *J. Geophys. Res. Space Physics*, 119,  
522 doi:10.1002/2013JA019296.
- 523 Huang, T.-Y. (2015). Gravity waves-induced airglow temperature variations, phase relationships, and  
524 krassovsky ratio for oh (8, 3) airglow, o<sub>2</sub> (0, 1) atmospheric band, and o (1s) greenline in the mlr region.  
525 *Journal of Atmospheric and Solar-Terrestrial Physics*, 130, 68–74.
- 526 Hunten, D. M. (1967). Spectroscopic studies of the twilight airglow. *Space Science Reviews*, 6 (4), 493–  
527 573.
- 528 Hunten, D. M., Turco, R. P., & Toon, O. B. (1980). Smoke and dust particles of meteoric origin in the  
529 mesosphere and stratosphere. *Journal of Atmospheric Sciences*, 37(6), 1342-1357.
- 530 Hunziker, H. E., & Wendt, H. R. (1974). Near infrared absorption spectrum of HO<sub>2</sub>. *The Journal of*  
531 *Chemical Physics*, 60(11), 4622-4623.
- 532 Janches, D., Swarnalingam, N., Plane, J., Nesvorny, D., Feng, W., Vokrouhlicky, D., & Nicolls, M. (2015).  
533 Radar detectability studies of slow and small zodiacal dust cloud particles. ii. a study of three radars with  
534 different sensitivity. *The Astrophysical Journal*, 807 (1), 13.
- 535 Kalashnikova, O., Horanyi, M., Thomas, G. E., & Toon, O. B. (2000). Meteoric smoke production in the  
536 atmosphere. *Geophysical research letters*, 27(20), 3293-3296.



- 537 Kero, J., Szasz, C., Nakamura, T., Meisel, D., Ueda, M., Fujiwara, Y., . . . Watanabe, J. (2012). The 2009–  
538 2010 mu radar head echo observation programme for sporadic and shower meteors: radiant densities  
539 and diurnal rates. *Monthly Notices of the Royal Astronomical Society*, 425 (1), 135–146.
- 540 Kero, J., Szasz, C., Pellinen-Wannberg, A., Wannberg, G., Westman, A., & Meisel, D. (2008). Three-  
541 dimensional radar observation of a submillimeter meteoroid fragmentation. *Geophysical Research*  
542 *Letters*, 35 (4).
- 543 Koch, J., Bourassa, A., Lloyd, N., Roth, C., She, C.-Y., Yuan, T., & von Savigny, C. (2021). Retrieval of  
544 mesospheric sodium from osiris nightglow measurements and comparison to ground-based lidar  
545 measurements. *Journal of Atmospheric and Solar-Terrestrial Physics*, 216, 105556.
- 546 Koschny, D., Soja, R. H., Engrand, C., Flynn, G. J., Lasue, J., Lévassieur-Regourd, A.-C., . . . others (2019).  
547 Interplanetary dust, meteoroids, meteors and meteorites. *Space science reviews*, 215 (4), 1–62.
- 548 Langowski, M. P., von Savigny, C., Burrows, J. P., Fussen, D., Dawkins, E., Feng, W., . . . Marsh, D. R.  
549 (2017). Comparison of global datasets of sodium densities in the mesosphere and lower thermosphere  
550 from gomos, sciamachy and osiris measurements and waccm model simulations from 2008 to 2012.  
551 *Atmospheric Measurement Techniques*, 10 (8), 2989–3006.
- 552 Leinert, C., & Grün, E. (1990). Interplanetary dust. In *Physics of the inner heliosphere i* (pp. 207–275).  
553 Springer.
- 554 Li, J., Williams, B. P., Alspach, J. H., & Collins, R. L. (2020a). Sodium resonance wind-temperature lidar at  
555 pfr: Initial observations and performance. *Atmosphere*, 11 (1), 98.
- 556 Li, Y., & Zhou, Q. (2019). Velocity and orbital characteristics of micrometeors observed by the arecibo  
557 430 mhz incoherent scatter radar. *Monthly Notices of the Royal Astronomical Society*, 486 (3), 3517–  
558 3523.
- 559 Li, Y., Zhou, Q., Scott, M., & Milla, M. (2020). A study on meteor head echo using a probabilistic  
560 detection model at jicamarca. *Journal of Geophysical Research: Space Physics*, 125 (1), e2019JA027459.
- 561 Li, Y., Zhou, Q., Urbina, J., Huang T.-Y., (2022). Sporadic micro-meteoroid source radiant distribution  
562 inferred from the Arecibo 430 MHz radar observations, *Monthly Notices of the Royal Astronomical*  
563 *Society*
- 564 Love, S., & Brownlee, D. (1993). A direct measurement of the terrestrial mass accretion rate of cosmic  
565 dust. *Science*, 262 (5133), 550–553.
- 566 Marsh, D. R., Janches, D., Feng, W., & Plane, J. M. (2013). A global model of meteoric sodium. *Journal of*  
567 *Geophysical Research: Atmospheres*, 118 (19), 11–442.
- 568 Mathews, J., Janches, D., Meisel, D., & Zhou, Q.-H. (2001). The micrometeoroid mass flux into the upper  
569 atmosphere: Arecibo results and a comparison with prior estimates. *Geophysical Research Letters*, 28  
570 (10), 1929–1932.
- 571 McBride, N., Green, S. F., & McDonnell, J. (1999). Meteoroids and small sized debris in low earth orbit  
572 and at 1 au: Results of recent modelling. *Advances in Space research*, 23 (1), 73–82.



- 573 Molod, A., Takacs, L., Suarez, M., & Bacmeister, J. (2015). Development of the GEOS-5 atmospheric  
574 general circulation model: Evolution from MERRA to MERRA2. *Geoscientific Model Development*, 8(5),  
575 1339–1356.
- 576 Nesvorný, D., Vokrouhlický, D., Pokorný, P., & Janches, D. (2011). Dynamics of dust particles released  
577 from Oort cloud comets and their contribution to radar meteors. *The Astrophysical Journal*, 743 (1), 37.
- 578 Nesvorný, D., Jenniskens, P., Levison, H. F., Bottke, W. F., Vokrouhlický, D., & Gounelle, M. (2010).  
579 Cometary origin of the zodiacal cloud and carbonaceous micrometeorites. Implications for hot debris  
580 disks. *The Astrophysical Journal*, 713(2), 816.
- 581 Plane, J. (2004). A time-resolved model of the mesospheric Na layer: constraints on the meteor input  
582 function. *Atmospheric Chemistry and Physics*, 4 (3), 627–638.
- 583 Plane, J., Oetjen, H., de Miranda, M., Saiz-Lopez, A., Gausa, M., & Williams, B. (2012). On the sodium D  
584 line emission in the terrestrial nightglow. *Journal of atmospheric and solar-terrestrial physics*, 74 , 181–  
585 188.
- 586 Plane, J. (2010). A reference atmosphere for the atomic sodium layer. *Atmos. Chem. Phys.*, 470 .
- 587 Plane, J. M., Daly, S. M., Feng, W., Gerding, M., & Gómez Martín, J. C. (2021). Meteor-ablated  
588 aluminum in the mesosphere-lower thermosphere. *Journal of Geophysical Research: Space Physics*, 126  
589 (2), e2020JA028792.
- 590 Plane, J. M., Feng, W., & Dawkins, E. C. (2015). The mesosphere and metals: Chemistry and changes.  
591 *Chemical reviews*, 115 (10), 4497–4541.
- 592 Qiu, S., Wang, N., Soon, W., Lu, G., Jia, M., Wang, X., . . . Dou, X. (2021). The sporadic sodium layer: a  
593 possible tracer for the conjunction between the upper and lower atmospheres. *Atmospheric Chemistry  
594 and Physics*, 21 (15), 11927–11940.
- 595 Robertson, H. (1937). Dynamical effects of radiation in the solar system. *Monthly Notices of the Royal  
596 Astronomical Society*, 97, 423.
- 597 Sugar, G., Marshall, R., Oppenheim, M., Dimant, Y., & Close, S. (2021). Simulation-derived radar cross  
598 sections of a new meteor head plasma distribution model. *Journal of Geophysical Research: Space  
599 Physics*, 126 (7), e2021JA029171.
- 600 Takahashi, T., Nozawa, S., Tsutsumi, M., Hall, C., Suzuki, S., Tsuda, T. T., . . . others (2014). A case study of  
601 gravity wave dissipation in the polar MLT region using sodium lidar and radar data. In *Annales  
602 geophysicae* (Vol. 32, pp. 1195–1205).
- 603 Vondrak, T., Plane, J., Broadley, S., & Janches, D. (2008). A chemical model of meteoric ablation.  
604 *Atmospheric Chemistry and Physics*, 8 (23), 7015–7031.
- 605 Yu, B., Xue, X., Scott, C. J., Jia, M., Feng, W., Plane, J., . . . Dou, X. (2022). Comparison of middle-and low-  
606 latitude sodium layer from a ground-based lidar network, the Odin satellite, and WACCM-NA model.  
607 *EGUsphere*, 1–34.



608 Zhou, Q. H., & Kelley, M. C. (1997). Meteor observations by the arecibo 430 mhz incoherent scatter  
609 radar. ii. results from time-resolved observations. *Journal of Atmospheric and Solar-Terrestrial Physics*,  
610 59 (7), 739–752.110

611

612

613

614

615

616

617

618

619

620

621